From GHz to mHz: A Multiwavelength Study of the Acoustically Active 14 August 2004 M7.4 Solar Flare

J.C. Martínez-Oliveros[1], H. Moradi[1], D. Besliu-Ionescu[1,2], A.-C Donea[1],
P.S. Cally[1], C. Lindsey[3]
[1] *Centre for Stellar and Planetary Astrophysics, School of Mathematical Sciences,*
Monash University, Australia (`juan.oliveros@sci.monash.edu.au`*)*
[2] *Astronomical Institute of the Romanian Academy, Bucharest, Romania*
[3] *NorthWest Research Associates, CORA Div. 3380 Mitchell Ln, Boulder, CO 80301*
USA

Abstract. We carried out an electromagnetic acoustic analysis of the solar flare of 14 August 2004 in active region AR10656 from the radio to the hard X-ray spectrum. The flare was a GOES soft X-ray class M7.4 and produced a detectable sun quake, confirming earlier inferences that relatively low-energy flares may be able to generate sun quakes. We introduce the hypothesis that the seismicity of the active region is closely related to the heights of coronal magnetic loops that conduct high-energy particles from the flare. In the case of relatively short magnetic loops, chromospheric evaporation populates the loop interior with ionized gas relatively rapidly, expediting the scattering of remaining trapped high-energy electrons into the magnetic loss cone and their rapid precipitation into the chromosphere. This increases both the intensity and suddenness of the chromospheric heating, satisfying the basic conditions for an acoustic emission that penetrates into the solar interior.

Keywords: Sun: magnetic field, Sun: flares, Sun: sun quakes, Sun: particle acceleration, Sun: helioseismology

1. Introduction

Wolff (1972) suggested for the first time that solar flares would release acoustic noise into the solar interior. He even suggested that these, and perhaps comets, were the primary source of solar oscillations discovered by Leighton, Noyes and Simon (1962). We know that most of the solar oscillations visible on the Sun's surface are too short-lived to be driven by flares, even at solar maximum, and are now believed to be driven by convection (Stein, 1967; Stein and Leibacher, 1974). Kosovichev and Zharkova (1998) suggested that large flares might produce sun quakes to be detected against the background of solar oscillations.

Kosovichev and Zharkova (1998) made the first identification of a sun quake, emanating from the X2.6 flare of 9 July 1996. The sun quake was assumed to be the signature of intense beams of high energy particles impinging into the lower solar atmosphere from the overlying corona. Donea, Braun, and Lindsey (1999) applied computational seismic holography to

helioseismic observations of the 9 July 1996 flare to make high-quality seismic images of its seismic source. Follow-up efforts to detect seismic emission from several other flares in 1998 and 1999, some considerably larger than the X2.6 flare of 9 July 1996, showed no other instances of significant acoustic emission (Donea and Lindsey, 2004). This made it evident that some flares are far more efficient emitters of seismic energy into the solar interior than others.

Recent developments in the study of flare acoustic emission (Kosovichev and Zharkova, 1998; Donea, Braun, and Lindsey, 1999; Donea and Lindsey, 2005) encourage the view that the seismic emission from flares is a major discovery with a broad range of diagnostic and control applications for helioseismologists and flare analysts. In order to study the effect of flares on solar oscillation modes, a ring-diagram technique has been used by Ambastha, Basu and Antia (2003) and Ambastha *et al.* (2004). They reported an increased power in the p-modes associated with the flaring region. At present, it is difficult to give a detailed comparison of these studies with the helioseismic holography results and a deeper analysis is required.

Helioseismology of "sun quakes," circular waves propagating outward along the solar surface from an impulsive flare $\approx 30 - 60$ minutes after the impulsive phase, offers us the opportunity to explore the acoustics of flares themselves as well as the subphotospheres of the active regions that produce them.

Donea and Lindsey (2005) produced seismic images of the seismic sources of the two large flares of $28 - 29$ October 2003. They suggested that photospheric heating could account for much of the seismic emission seen and that this may be the result of high-energy protons, which were evident from characteristic γ-ray signatures seen by RHESSI in the flares of $28 - 29$ October 2003. However, the flare of 15 January 2005 (an X1.2 class flare) showed no signature of protonic γ-rays. This led Donea *et al.* (2006) and Moradi *et al.* (2007) to suggest that the photospheric heating that they supposed would drive the seismic transient might have been the result of back-warming by the downward emitted component of intense Balmer and Paschen continuum radiated from the overlying heated chromosphere (Hudson, 1972; Metcalf *et al.*, 2003).

Sun quakes are not extremely rare, and they emanate from compact sources that represent only a small fraction of the energy emitted from flares. Donea and Lindsey (2005) considered the possibility that relatively weak flares might be able to produce detectable sun quakes and that acoustically active flares might indeed be much more common than previously thought. This has turned out to be the case, as a comprehensive survey of helioseismic observations of flares from the Michelson-Doppler Imager (MDI) aboard the Solar Heliospheric Observatory (SOHO) covering a significant fraction of

solar activity cycle 23 by Donea *et al.* (2005) and Besliu-Ionescu *et al.* (2006) has shown.

Indeed, on 9 September 2001 at 20:40 UT, an M9.5 flare occurred in active region AR 9608. Donea *et al.* (2006) have extensively analysed the seismic transient of this flare. The helioseismic signatures of this flare drew our attention to several important points: the acoustic signature of the flare was quite compact and was spatially and temporally consistent with the white-light signature, reinforcing the suggestion that sudden heating of the photosphere may contribute significantly to the seismic emission detected. They also found that the acoustic signature was spatially and temporally coincident with suddenly changing magnetic signatures, suggesting that suddenly changing magnetic forces might have contributed to the seismic emission.[1] The fraction of energy emitted into the subphotosphere as seismic waves remained a small fraction of the total energy released in the flare. The persistence of a sudden, co-spatial white-light signature in flares where no energetic protons were evident was consistent with acoustic emission driven by back-warming of the low photosphere by radiation from a heated overlying chromosphere.

In this paper, we report the discovery of a seismic transient produced by the M7.4 solar flare of 14 August 2004 in AR 10656. We have derived phase-coherent seismic images of the source of this flare from Doppler seismic observations of the flare by the MDI using computational seismic holography. Other supporting hard X-ray observation data included in this study are from the Reuven Ramaty High Energy Solar Spectroscopic Imager (RHESSI), soft X-ray emission from the Geostationary Operational and Environmental Satellites (GOES), visible continuum emission from the Global Oscillations Network Group (GONG+), Hα emission from the Big Bear Solar Observatory (BBSO) and radio emission from the Nobeyama Radio Heliograph (NoRH). We will compare these observations with the holographic images.

2. The Helioseismic Observations

The MDI data we utilised consist of full-disk Doppler images in the photospheric line Ni I 6768 Å, obtained at a cadence of 1 minute, in addition

---

[1] Donea *et al.* (2006) and Moradi *et al.* (2007) have expressed concern as to whether the magnetic signatures are the result of real changes in the photospheric magnetic field. Kosovichev and Zharkova (2001) also reported similar magnetic signatures in flares. They expressed concerns about possible effects of an inversion of the Ni I 6768 Å line as a result of heating of the solar atmosphere by high-energy particles. Sudol and Harvey (2005) likewise found transient magnetic signatures in flaring photospheres. Qiu and Gary (2003) attribute the sign reversal in the MDI magnetic signature of an impulsive flare to radiative-transfer effect. Clearly, these are concerns that need to be considered.

to approximately hourly continuum intensity images and line-of-sight magnetograms. The MDI data sets are described in more detail by Scherrer *et al.* (1995). For the flare of 14 August 2004, we analysed a dataset with a period of 4 hours around the time of the flare. We also obtained visible continuum maps of AR10656 during the flare from the GONG observatory at Mauna Loa. Technically, the GONG "continuum intensity maps" represent a measure of radiation in a $\approx$0.7 Å bandpass centred on the Ni ɪ 6768 Å line, whose equivalent width is 0.07 Å.

For the purpose of our analysis, all MDI and GONG images were remapped as a Postel projection (DeForest, 2004) that tracks solar rotation, with the region of interest fixed at the center of the projection. The nominal pixel separation of the projection was 0.002 solar radii (1.4 Mm) with a 256×256 pixel field of view.

3. The Acoustic Signatures

AR10656 first appeared on the solar surface on 7 August 2004 at S12E55 $(-758'', -253'')$ as an α sunspot. Over the next seven days, the active region continued to increase in magnetic complexity and evolved to a $\beta\gamma\delta$ type. During the period $8-16$ August it produced 2 X-class, 36 M-class and more than 150 C-class solar flares.

On 14 August, the active region was situated at S13W36 $(542'', -298'')$ and was characterised by a strong δ configuration in the center of the sunspot, and an overall configuration of $\beta\gamma\delta$. At 05:36 UT an M7.4-class solar flare occurred, peaking at 05:44 UT and concluding at 05:52 UT (as given by GOES12) with an X-ray flux of 3.8×10^{-2}J m^2. This flare produced significant seismic emission, and is the least energetic flare in soft X-rays known to have generated a detectable acoustic transient.

It should be emphasised that the same active region produced two other significant seismic transients within a period of 48 hours: the first was generated by an X1.0 flare on 13 August 2004; the second was generated by the M9.4 solar flare on 15 August 2004 (Besliu-Ionescu *et al.*, 2006; Donea *et al.*, 2006). We applied computational seismic holography to the helioseismic observations to image the acoustic sources of these sun quakes. This method is described in depth by Lindsey and Braun (2000), and has been used extensively in flare seismology, with great success in identifying numerous seismic sources from solar flares (Donea, Braun, and Lindsey, 1999; Donea and Lindsey, 2005; Donea *et al.*, 2006; Moradi *et al.*, 2007). Helioseismic holography is essentially the phase-coherent reconstruction of acoustic waves observed at the solar surface into the solar interior to render stigmatic images of subsurface sources that have given rise to the surface disturbance. Because the solar interior refracts down-going waves back to the surface,

helioseismic holography can likewise use observations in one surface region, the pupil, to image another, the focus, a considerable distance from the pupil. This is referred to as "seismic holography from the subjacent vantage" (Lindsey and Braun, 2000). The subjacent vantage renders the photosphere as viewed by an acoustic observer directly beneath it. In general the acoustic reconstruction can be done either forward or backward in time. When it is backward in time, we call the extrapolated field the "acoustic egression." In the case of subjacent vantage holography, this represents waves emanating from the surface focus downward into the solar interior.

To assess seismic emission from the flare, we computed the egression over the neighborhood of the active region at 1-minute intervals, mapping the egression power for each minute of observation. The resulting egression power movies and "snapshots" (egression power sampled over the solar surface at any definite time) are computed over 2 mHz bands, centred at 3 mHz and 6 mHz. The higher frequency band has a number of advantages in that it avoids the much greater quiet-Sun ambient noise that predominates the $2-4$ mHz frequency band and due to a shorter wavelength, it also provides us with images that have a finer diffraction limit. However, these advantages come at some expense in temporal discrimination, as the temporal resolution of egression computations is limited to

$$\Delta t \;=\; \frac{1}{\Delta \nu} \;=\; \frac{1}{2 \text{ mHz}} \;=\; 500 \text{ s}. \tag{1}$$

This temporal smearing results in the acoustic signature of the flare commencing several minutes before the actual onset of the flare and lasting for several minutes afterward, even if the actual acoustic disturbance was instantaneous.

Egression power snapshots before, during and after the flare are shown in the last three rows of Figure 1 at 3 mHz (left column) and 6 mHz (right column). In these computations the pupil was an annulus of radial range $15-45$ Mm centered on the focus. To improve the statistics, the original egression power snapshots are smeared by convolution with a Gaussian with a $1/e$-half-width of 3 Mm. The egression power images and the continuum images are also normalised to unity at respective mean quiet-Sun values. At 3 mHz this is $\sim$2.0 kW m^{-2}. At 6 mHz it is 70 W m^{-2}.

All egression power snapshots mapped in Figure 1 show considerably suppressed acoustic emission from the magnetic region, attributed to strong acoustic absorption by magnetic photospheres, discovered by Braun, Duvall and LaBonte (1988) (see also Braun, 1995; Braun et $al.$, 1998; Braun and Lindsey, 1999a). Furthermore, all 6 mHz egression power snapshots in Figure 1 show acoustic emission "halos," $i.e.$ significantly $enhanced$ acoustic emission from the outskirts of complex active regions (Braun and Lindsey, 1999b; Donea, Braun, and Lindsey, 1999).
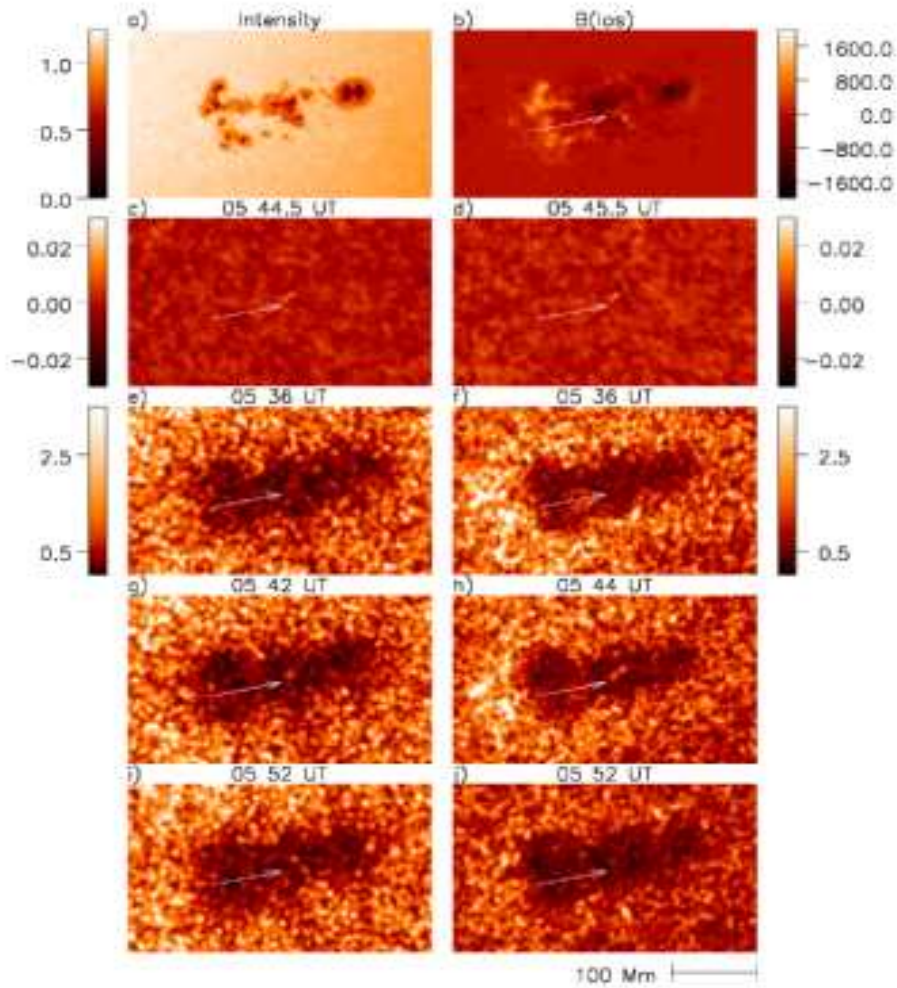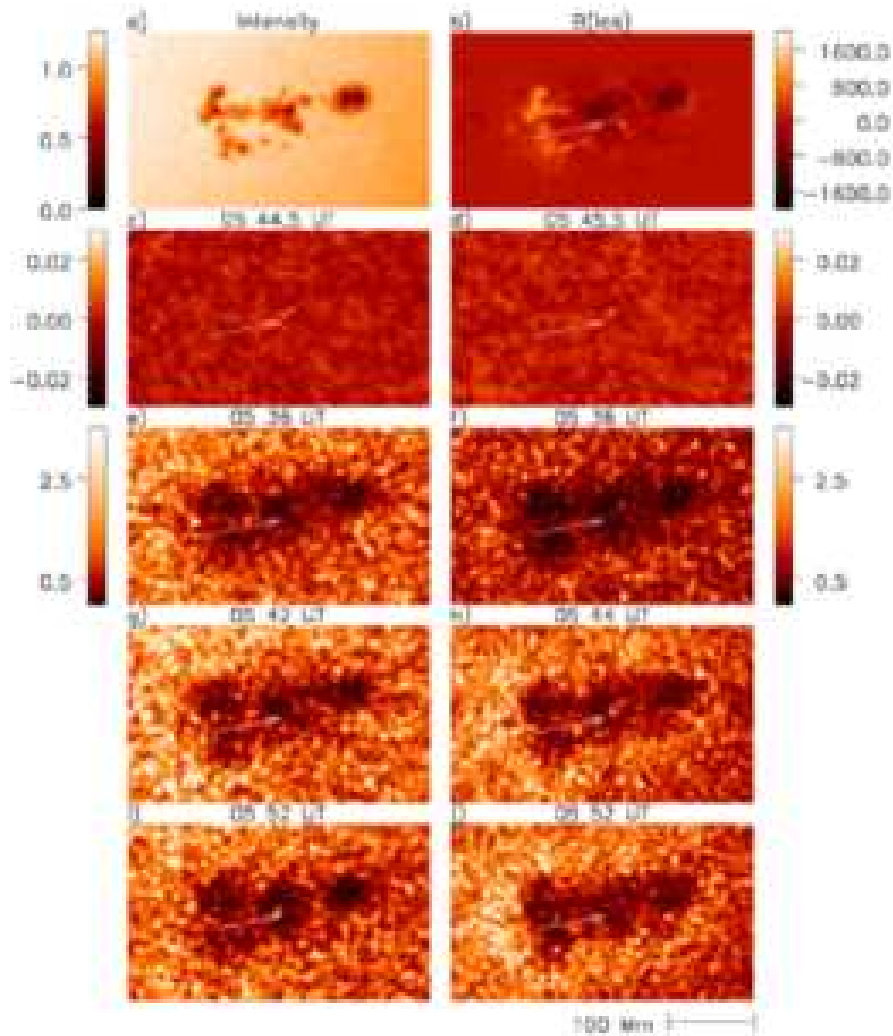
Figure 1. Egression power snapshots of AR10656 on 14 August 2004 taken before, during and after the flare and integrated over a $2.0 - 4.0$ mHz and $5.0 - 7.0$ mHz frequency band. Top frames show a MDI visible continuum image of AR10656 (left) at 06:24 UT and a magnetogram (right) at 05:44 UT. Second row shows GONG continuum intensity differences 30 seconds before and after the time that appears above the respective frames. Bottom three rows show egression power maps before (row 3), during (row 4), and after (bottom row) the flare at 3 mHz (left column) and 6 mHz (right column). Times are indicated above respective panels, with arrows inserted to indicate the location of the acoustic source. Color scales at right and left of row 3 apply to respective columns in rows $3 - 5$. The seismic region is easily seen in a movie of the egression power maps. For a better visualisation of the acoustic source, we have enhanced the area of the seismic signature by a factor of 1.5.
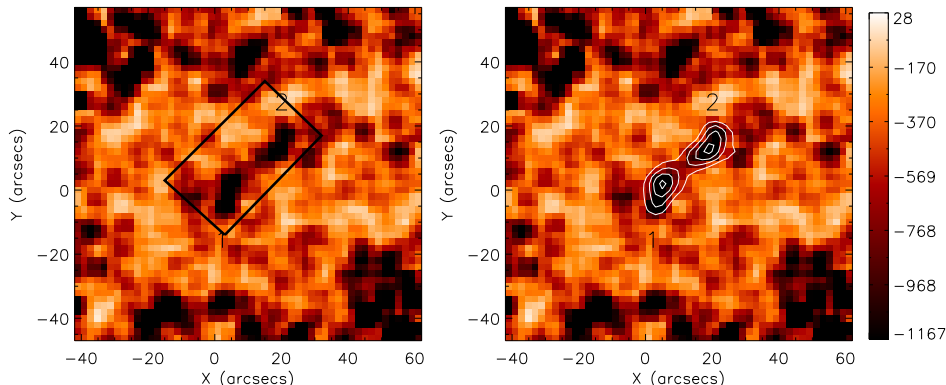
Figure 2. A zoom image of the 6 mHz egression power snapshot seen in Figure 1(h) taken at 05:44 UT. The color map of the image was inverted for a better visualisation of the acoustic source morphology. The left panel shows the acoustic kernels (labelled 1 and 2) and the right panel shows the same image but with egression power contours overlaid. The acoustic source 1 appears to be the stronger of the two. The rectangle represents the seismic region which we used in this paper to study the time series.

Looking at Figure 1, a significant excess of acoustic emission is evident at 05:44 UT in the 6 mHz egression power snapshot, indicated by an arrow in all of the frames, appearing to lie across the penumbral magnetic neutral line and spanning $\approx$25 Mm in length. Upon closer inspection, we can see from the zoomed egression power snapshot in Figure 2, that there are in fact two separate components to the seismic source (acoustic kernels) that appear to be separated by $\approx$7 Mm when they initially appear (05:39 UT), and because of their close proximity and evolution with time, they seem to appear as one extended source in Figure 1. These acoustic kernels coincide closely with hard X-ray (HXR) signatures (see Section 4.4 and Figure 14), indicating that high-energy particles accelerated above the chromosphere contribute to the excitation of the seismic source. The egression power map in Figure 2 is smeared by a factor of 0.004, in order to emphasise the source geometry and the acoustic kernels. The map also shows kernels that we associate with the fluctuating acoustic noise of the active region.

The source geometry also closely corresponds with other compact manifestations of the flare including significant white-light emission with a sudden onset, as indicated by the intensity difference signatures shown in the second row of Figure 1, and microwave emission at 17 and 34 GHz. The 3 mHz egression power snapshots (Figure 1) also shows emission during the flare. In fact, from the egression and acoustic power time series of Figure 4, it appears that we have a distinct and considerably stronger seismic emission at 3 mHz

Figure 3. Acoustic power snapshots of AR10656 on 14 August 2004. Details are the same as for Figure 1, but local acoustic power maps appear in the bottom three rows in place of egression power maps.

than at 6 mHz. This is because of a much greater ambient acoustic noise at 3 mHz which renders the considerably greater 3 mHz seismic emission signature no more conspicuous than 6 mHz.

Figure 3 shows the local acoustic power snapshots of AR10656 at 3 mHz (left column) and 6 mHz (right column) before, during and after the flare. Each pixel in a local acoustic power map represents the local surface motion
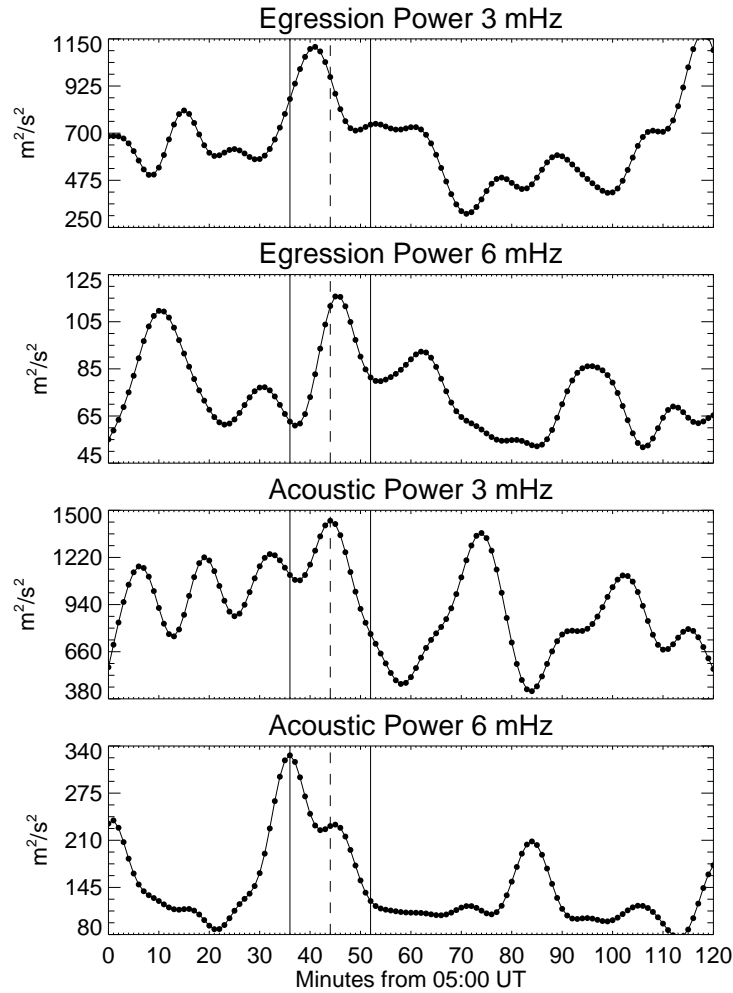
Figure 4. 3 and 6 mHz egression power and acoustic power time series, integrated over the neighborhood of the egression power signatures, are plotted in the top four rows. The vertical lines represent the beginning (05:36 UT), maximum (05:44 UT) and ending (05:52 UT) times of the GOES X-ray flare. The relatively extended duration of the acoustic signatures is a result of limits to temporal resolution imposed by truncation of the spectrum (see equation 1).

as viewed directly from above the photosphere, which should not be confused with the egression power computed by subjacent vantage holography of the surface, where each pixel is a coherent representation of acoustic waves that have emanated downward from the focus, deep beneath the solar surface, and re-emerge into a pupil $15-45$ Mm from the focus. As in the case of the 6 mHz egression power, the local acoustic power maps show a broad acoustic deficit marking the magnetic region and an enhanced local acoustic power halo surrounding the active region which is also clearly apparent. The acoustic source is difficult to distinguish in either the 3 or 6 mHz acoustic power signatures.

4.   Analysis and Results

4.1.   White Light Flare signature

Figure 5 shows the time dependence of the visible continuum irradiance normalised to the quiet-Sun and integrated over the area of the seismic source. At 05:39 UT the irradiance began to increase for $\sim$4 minutes, then underwent a sudden jump at 05:42 UT for approximately 2 minutes and then slowly decreased to the background level. The maximum irradiance was approximately 4% above the quiet-Sun mean.
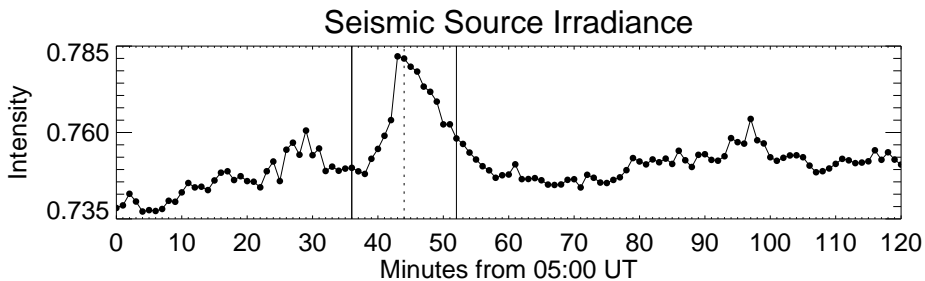
Figure 5. Time dependence of the visible continuum irradiance normalised to the quiet-Sun and integrated over the area of the seismic source. The vertical lines show the flare times as in Figure 4. The maximum emission in white light continuum temporally coincides with the 6 mHz seismic emission at its maximum.

The white light flare signature is spatially co-aligned with the emission of the seismic sources as imaged in Figure 1.

4.2.   The Magnetic Field

Schunker *et al.* (2005) have shown that magnetic forces are of particular significance for acoustic signatures in penumbral regions, where the magnetic field is significantly inclined from vertical. Therefore, understanding

the 3-D magnetic configuration of the coronal loops hosting flares would give us a powerful control utility for seismic diagnostics of active region sub-photospheres. This will be useful for addressing questions concerning the MHD of inclined magnetic fields, the role of fast and slow magneto-acoustic mode coupling in magnetic photospheres, sub-photospheric thermal structure, and how wave generation by turbulence in active region sub-photospheres differs from that in the quiet sub-photosphere.

In Figure 6 we have shown the time series of the mean and the root mean square (RMS) values of the line-of-sight (LOS) magnetic field, integrated over area of the seismic source (the integration area is plotted in Figure 2 - black rectangle - and its area has a value of $\approx$247 Mm^2). The vertical lines mark the time frame of the flare.
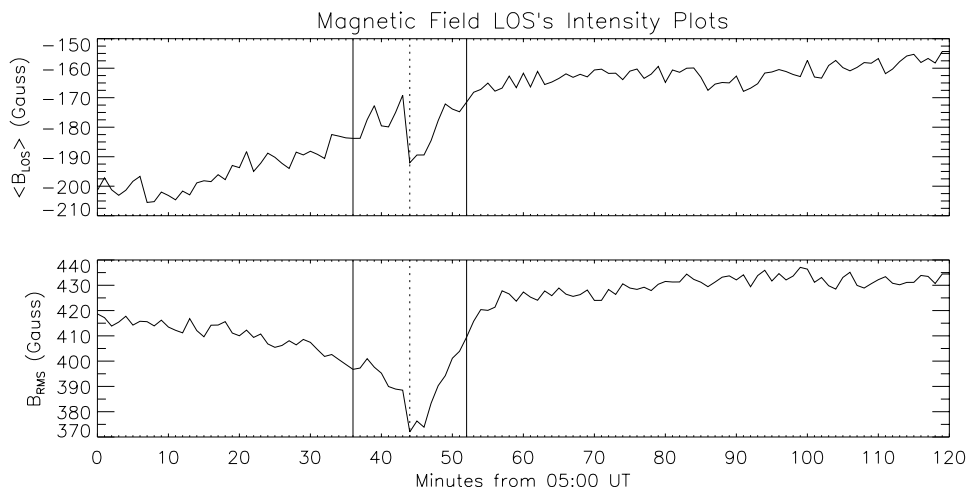

Figure 6. Time series of the mean and the root mean square of the LOS magnetic field integrated over the area of the seismic source.

The mean LOS magnetic field shows a steady increase from 05:10 to 06:00 UT with a strong variation as a sudden decrease, at the maximum of the flare (05:44 UT). The RMS of the magnetic field intensity shows a sudden decrease of about 9.6% of the background level, and a sudden recovery to a 3.6% increased background, as compared to the background level before the flare (similar changes have been observed by Kosovichev and Zharkova, 2001; Sudol and Harvey, 2005; Ambastha, Hagyard and West, 1993; Wang et al., 2005; see also the footnote 1 for more references.). To obtain a general idea of the configuration of the coronal magnetic field lines in AR10656 we computed the potential field extrapolation by applying the code described in Sakurai (1982) to the MDI line-of-sight magnetogram. According to this extrapolation (Figure 9, top frame), the field lines whose footpoints were planted in the general region of the acoustic emission were relatively low and

compact, suggesting that the magnetic loops, into which particle acceleration occured during the reconnection, were relatively short. The second panel in Figure 9 shows the appearance after the flare maximum of more magnetic field lines connecting the positive and negative polarities. A small difference in the line-of-sight magnetic field configuration in the region of the acoustic emission described by the inclined rectangle is also noticeable.
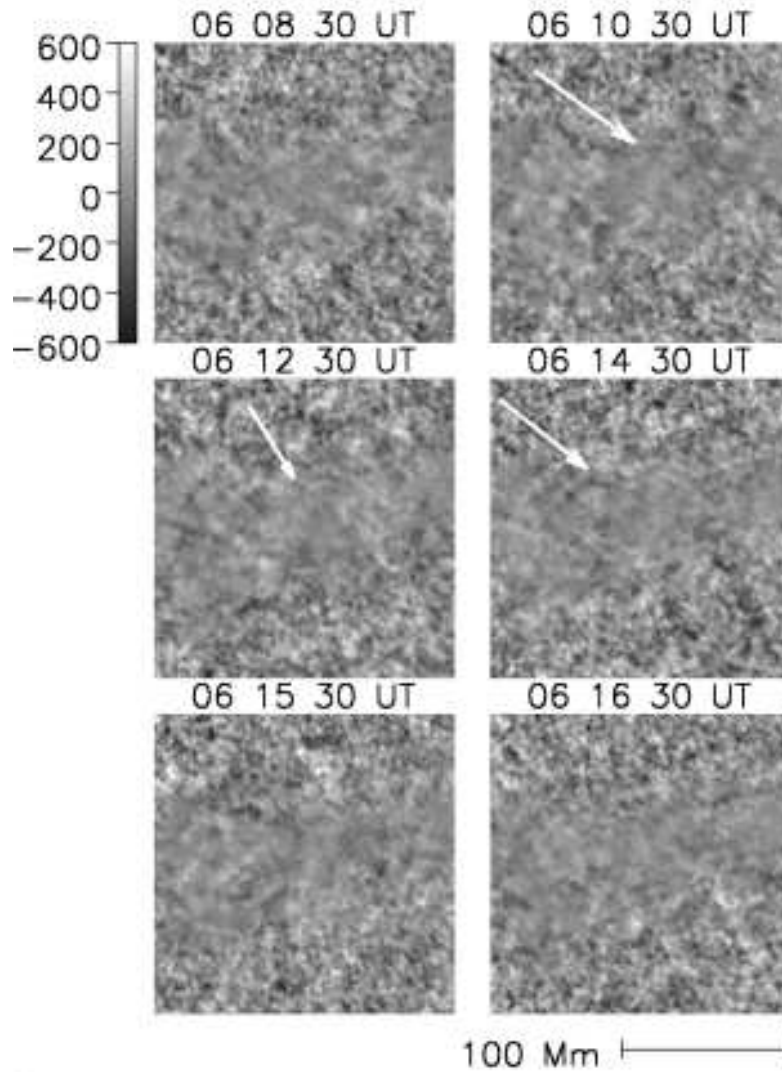
4.3. The Surface Ripple

We computed differences between consecutive Doppler frames, separated by one minute in time, around the time of the flare to reconstruct time-distance profiles of this seismic emission. In this sequence we see a surface ripple propagating in the North direction, over the range $-50°$ to $+20°$ from due north in a reference frame centered on the seismic source. The surface ripple represents acoustic waves that propagated tens of Mm into the solar interior from the acoustic source and were refracted back to the surface 30 minutes after the impulsive phase of the flare. Because of the strong fluctuating motions of the background, the ripple is difficult to see in individual dopplergrams. They are easily recognised in a movie of differences of consecutive Doppler frames. Even so, we are able to see the ripple at approximately 06:10 – 06:15 UT. The arrows in Figure 7 indicate their location. The ripples expand into the north quiet Sun before becoming submerged into the ambient noise. We do not see an expanding wave moving southward, either because the signal is too weak to be detected by eye or the emission to the north is simply stronger. The seismic wave is highly anisotropic, its amplitude varies with angle. The strongest amplitude is observed in the north direction. In section 4.4 we will see that this direction is also approximately the direction of the motion of HXR footpoints. A similar behaviour was reported by Donea and Lindsey (2005) in the seismically active flares of the October 2003. The fronts of the eastern, southern and western acoustic seismic wave propagate through the sunspot, and are exposed to a strong local magnetized environment. As a result a significant decay and some distortion is expected, weakening the surface ripple.

Figure 8a shows a time-distance amplitude profile for the ripple described above. The Doppler difference amplitude was averaged along curves of constant radius in the reference frame described above over the -50 to $+20°$ range of azimuths over which the surface ripple was visible. This resulting gray-tone plot is shown in Figure 8(b) with the theoretical group travel time plotted for reference.[2]

---

[2] This travel time, $t(\rho)$, is defined by the path integral

$$t(\rho) \;=\; \int_{\Gamma(\rho)} \frac{ds}{c}, \tag{2}$$

Figure 7. Observations of surface ripples at the specified times emanating from AR10656 following the impulsive phase of the flare. Arrows show the location of the surface ripples. Only the north angular sector of the ripple can be seen by eye.

4.4. RADIO AND HXR EMISSION

The flare of 14 August 2004 was observed with the Nobeyama Radio He-liograph (NoRH), at 17 GHz and 34 GHz, and the Reuven Ramaty High Energy Solar Spectroscopic Imager (RHESSI). Unfortunately, the totality

---

where Γ represents the path of least time through the quiet subphotosphere connecting surface points separated by an angular distance ρ along the surface.
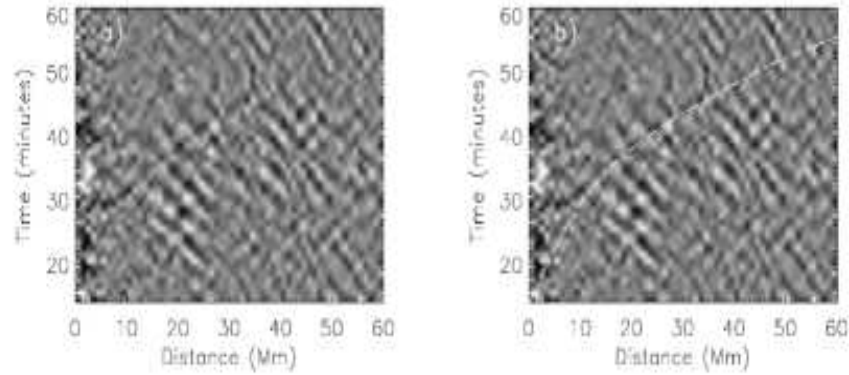
Figure 8. Time-distance propagation amplitude of the surface ripple averaged over curves of constant radius, over azimuths from -50 to $+20°$ is rendered in gray tone in both frames. The curve superimposed in the right frame represents the wave travel time, t, for a standard model of the solar interior. The time 05:30 UT is represented by $t = 0$.

of the impulsive and main phases of the flare was not observed by RHESSI, and as a result, images and time profile of the hard X-ray (HXR) emission just prior to, and after the maximum of the flare, are not available.

Figure 10 shows the total flux time profiles of the event in microwaves, soft and hard X-rays. The GOES total fluxes in the two channels $1-8$ Å and $0.5-4$ Å are shown in the top graph of Figure 10. Figure 10b shows the HXR-RHESSI time profile in the two channels $15-25$ keV (black line) and $25-50$ keV (red line). Figure 10c shows the microwave time profiles obtained using the Nobeyama Radio Polarimeter (NoRP) data at 17 GHz (red line) and 35 GHz (black line). In Figure 10d, we plotted the normalised total GOES flux at $1-8$ Å and the NoRP flux at 35 GHz. The empirical relation observed between the soft X-rays flux and the HXR or microwaves is called the Neupert effect (Neupert, 1968). It is clear from Figure 10d, that this effect is present and that the NoRP 35 GHz emission lags behind the GOES soft X-ray by 43 seconds. The microwave emission did not present a significant thermal component, suggesting relatively inefficient trapping of the accelerated electrons in the coronal magnetic field. This result is of significant importance to the process of transportation of energy from the reconnection site into the lower layers of the chromosphere and further into the photosphere where the sun quake was produced.
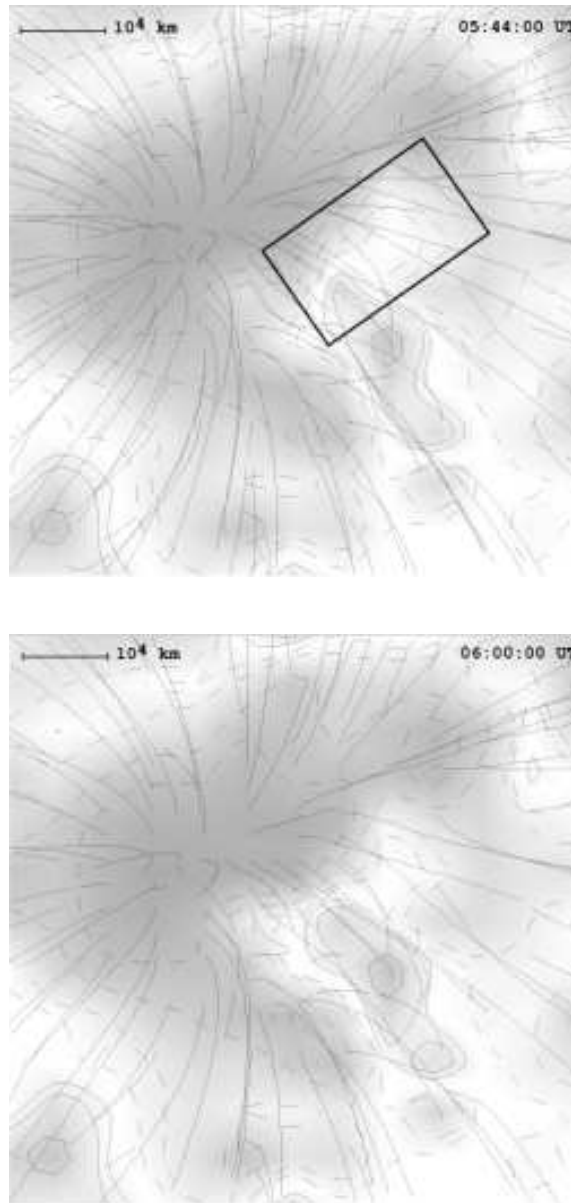
Figure 9. Potential magnetic field extrapolation of SOHO-MDI magnetograms. Top: Magnetic field extrapolation at 05:44:00 UT. Bottom: Magnetic field extrapolation at 06:00:00 UT. The grayscale background image shows the absolute value of the line-of-sight magnetic field. The dashed lines represent the negative magnetic polarity, while the solid lines represent the positive magnetic polarity. The contour lines levels are 50, 100, 300, 500, 1000 G. In the image North is up, the dimension are 104 by 104 arcsec centred at (462,−303) arcsec.

It has already been established that a close relationship exists between HXR and radio fluxes in the impulsive phase of a flare (see Kundu *et al.*, 2001; Bastian *et al.*, 1998). Based on this relationship, it is generally believed that essentially the same population of energetic electrons is responsible for both HXR and radio emission. The radio emission is thought to be produced by accelerated nonthermal electrons orbiting magnetic field lines and trapped in the coronal magnetic field. The hard X-ray emission is produced by Coulomb collisions of these energetic electrons with the dense chromospheric plasma.
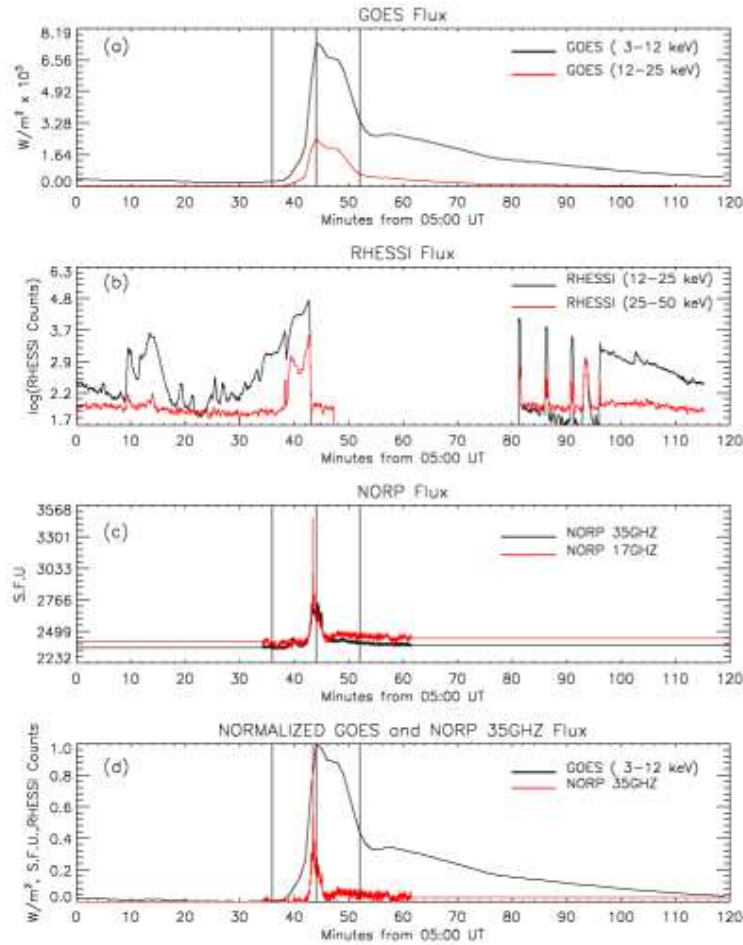
Figure 10. Integrated flux time profiles: a) GOES soft X-ray $1-8$ Å and $0.5-4$ Å channels; b) RHESSI time profiles in two channels $12-25$ keV (black line) and $25-50$ keV (red line); c) Microwave time profiles at 17 (red line) and 35 GHz (black line); d) Normalised total GOES total flux (black line) and microwave flux at 35 GHz (red line). The vertical lines show the beginning, maximum and end of the event.

The maximum brightness temperature of the radio source at 17 GHz (Figure 11, left panel) was measured to be 4.67×10^7 K, with a spectral index, δ, of -3.67. These results indicate that a non-thermal emission process for the microwave radiation is at work; the non-thermal emission region was also confirmed using the variance technique[3] for solar radio image analysis (Grechnev, 2003). This technique allows us to plot a radio map of the non-thermal emission from the active region by also subtracting any contribution from thermal sources in the corona. From the variance map (Figure 11, right panel) we infer that the non-thermal emission is compact and well correlated with the HXR emission region. The flux of electrons with energies $\gtrsim 25$ keV is very small, $\approx 6\%$ of the flux registered in the $12-25$ keV energy band, and possibly did not make a significant contribution to the seismic emission. A delay of 43 seconds is observed between the microwave emission (05:43:17 UT) and the maximum in the seismic signature (05:44:00 UT). A similar delay is observed between the NoRP 35 GHz emission and the GOES soft X-ray.
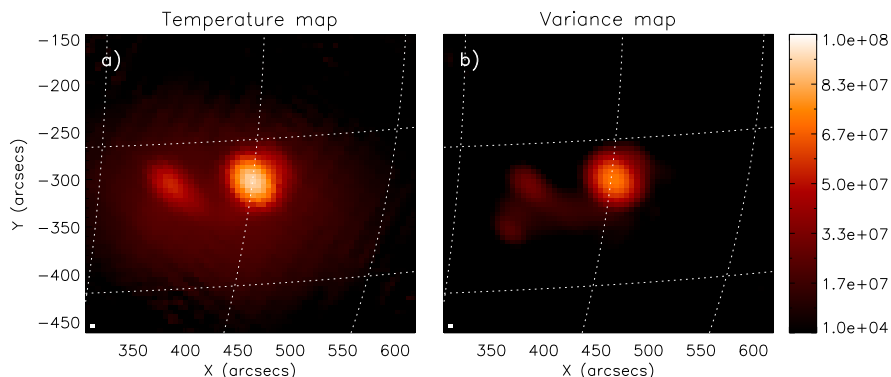

Figure 11. Temperature and variance maps. Panel (a) shows the brightness temperature radio map at 17GHz and panel (b) shows the variance map, which identifies a non-thermal radio source at the location of the main spot of the AR10656.

Figure 12 shows a sequence of images of the 14 August 2004 flare taken by the Transition Region and Coronal Explorer (TRACE) overplotted with the contours of the NoRH microwave emission at 17 GHz (large red contours) and RHESSI $12-25$ keV HXR (small black contours). We applied the MEM-SATO algorithm (Sato, Kosugi and Makishima, 1999) available

---

[3] We calculate a variance map of a set of radio images using the following equation:

$$\sigma_{ij}^2 = \frac{1}{N} \sum_{k=1}^{N} x_{ijk}^2 - \frac{1}{N^2} \left(\sum_{k=1}^{N} x_{ijk} \right)^2 \tag{3}$$

where $i = 1, 2, \ldots, L$ is the image row number, $j = 1, 2, \ldots, M$ the column number and $k = 1, 2, \ldots, N$ is the image number in the data set.
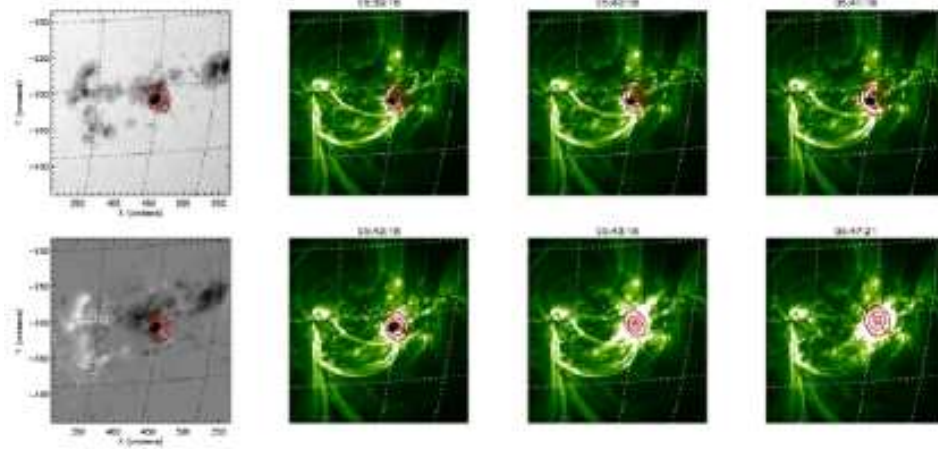
Figure 12. First column shows the MDI intensity continuum and magnetogram images of AR10656 with the microwave emission at 17 GHz (red large contours) and RHESSI 12 – 25 keV (black small contours) overplotted. Evolution of the flare at 171Å as observed by TRACE is shown in the last three columns for the specified times. RHESSI 12 – 25 keV HXR emission (black contours) with contour levels of 50%, 80% and 95% of the maximum source intensity, and NoRH microwave emission at 17 GHz (red contours) at 20%, 50%, 80% and 95% of the maximum intensity of the radio source are also shown. The field of view is $256'' \times 256''$ with north is upward.

in the standard RHESSI software to reconstruct RHESSI images from grids 3, 4, 5, 6, and 8 using an integration time of 1 to 4 s. As seen in Figure 12, the impulsive phase of the flare has a simple compact morphology in both HXR and microwaves until the minute prior to the flare maximum, when the HXR source evolves into an extended source composed of three smaller kernels (as seen in Figure 13). The radio source maintained its morphology after the flare maximum. The close temporal and spatial correlation between the microwave and X-ray emissions in this flare indicates a sudden energy deposition into the chromosphere by non-thermal electrons. This is in agreement with the prediction made by Kosovichev and Zharkova (1998). Figure 12 also shows a spatial correlation between the flare region observed by TRACE at 171 Å and the microwave and HXR sources.

The temporal evolution of the HXR feature, with respect to the photospheric magnetic neutral line, can be seen over a sequence of MDI magnetograms taken around the time of flare-maximum (Figure 13). The HXR footpoint appears to be moving in the north – north – east direction, a motion which is not parallel to the photospheric neutral line. Furthermore, we can clearly see that the source maintains its compact HXR structure until the last minute of observation (05:42 UT), reinforcing the observations shown in Figure 12. In this last minute, the source appears to evolve into an elongated shape that covers both magnetic polarities lying around the
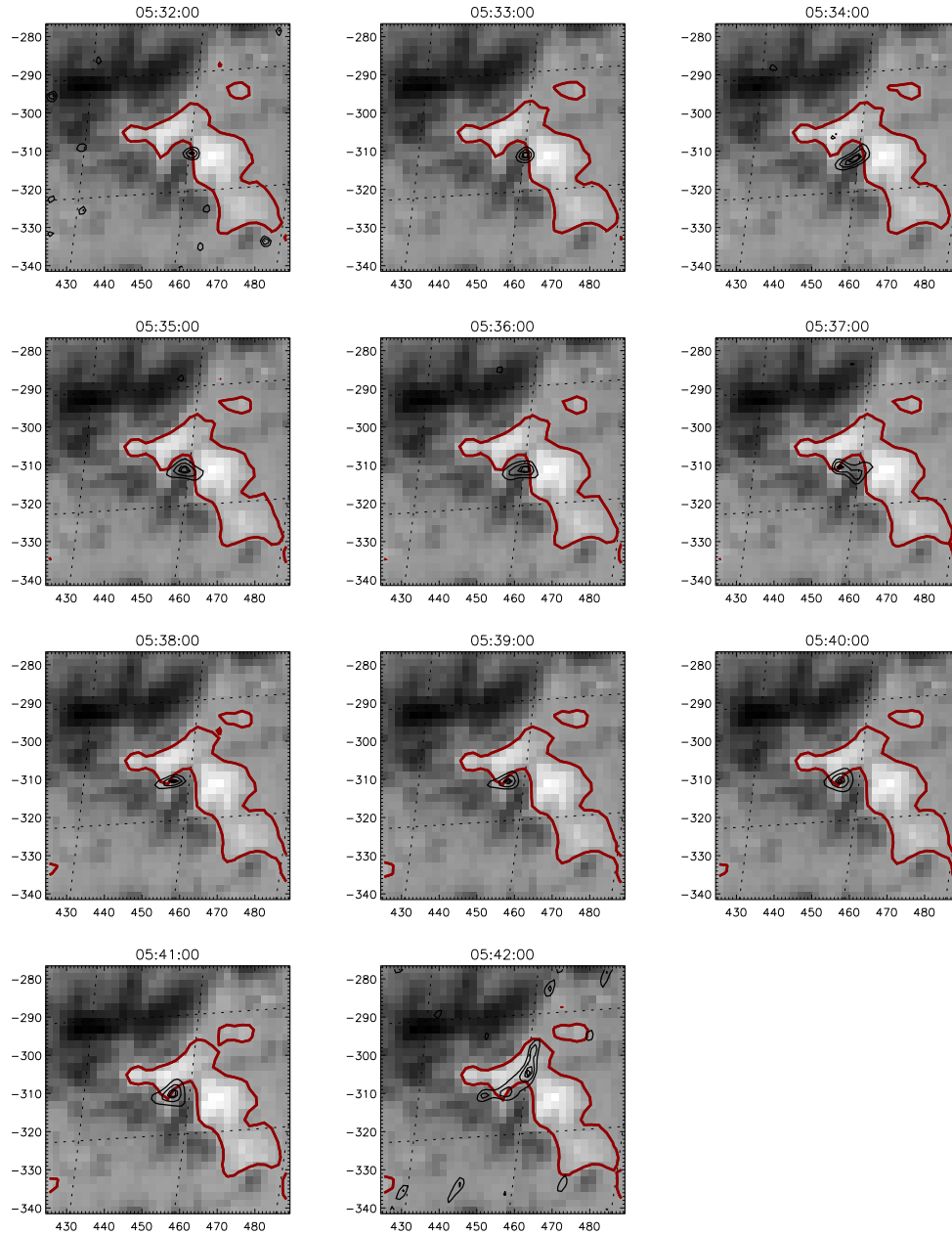
Figure 13. Evolution of the MDI magnetogram (background) and RHESSI-HXR source 12 – 25 keV (black contours, with levels 50%, 80% and 95% of the maximum source intensity) from 05:32:00 UT to 05:42:00. The red line is the magnetic neutral line of the MDI magnetogram. North is up and East to the left.

neutral line. This new elongated source is composed of three kernels, two
of which are located in the positive magnetic region and the third one is
located near the final position of the compact source observed at 05:42 UT.
We remark that the motion and evolution of the RHESSI source is seen as
projected over the egression power maps. The frames in Figure 13 show first
a loop-top emission (compact kernel) which gradually moves towards the
footpoints along a single magnetic loop, the one that hosted the seismically
active flare. The break-up of the HXR emission kernels began at 05:42 UT.
After this time, no RHESSI data where available, but following a similar
study done by Donea and Lindsey (2005), we can predict that the RHESSI
footpoints and the seismic source will match in the following two minutes.
Figure 14 shows that the egression power snapshot at 6 mHz and the HXR
sources have a similar morphology, with two of the four HXR sources (fp1
and fp2 in Figure 14) having a strong spatial correlation with the acoustic
kernel sources in the egression power snapshot.
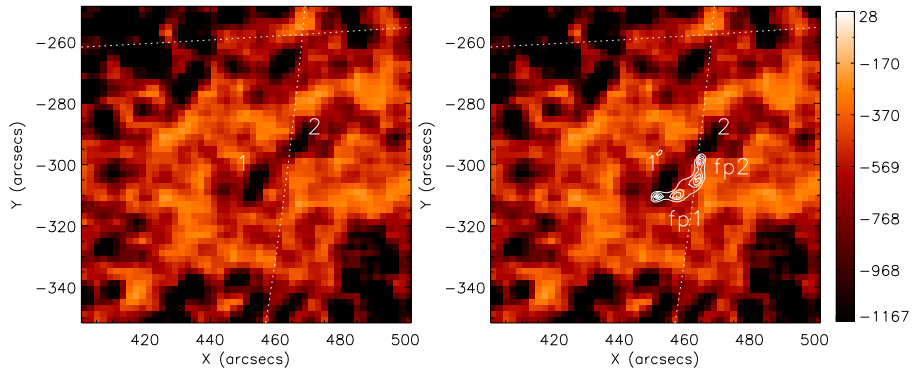
Figure 14. Left: Egression power map at 6 mHz, with contour levels of 50%, 65%, 80% and
95% of the maximum source intensity. Right: Egression power map and RHESSI contour
plots, with levels of 30%, 50%, 70% and 90% of the maximum source intensity. The color
map of the egression power map was inverted for a better visualisation of the acoustic
source.

5.   Conclusions

The detection of seismic transients from the M-class flares opens a new era
of studying seismically active solar regions. Acoustically active flares are the
most compact, most impulsive, and highest-frequency solar acoustic sources
discovered to date. Moreover, they are the only known sources of acoustic
waves that operate in the outer, visible, solar atmosphere. This makes the

transients they release into active region sub-photospheres understandable in a way that wave generation by sub-photospheric convection is not.

We carried out a study of the M-class flare of 14 August 2004 from AR10656, including HXR emission, seismic emission into the solar interior in the $2.5 - 7.0$ mHz spectrum and radio emission up to 34 GHz. We applied holographic and other standard time-distance diagnostics to helioseismic observations of the seismic transient emitted by the flare. These clearly show the signature of an expanding wave packet centered on a source of HXR emission. The holographic images show a seismic source morphology composed of two kernels approximately perpendicular to the magnetic neutral line of the active region in the penumbra of one of the sunspots. The kernels are spatially aligned close to similar HXR kernels in the $12 - 25$ keV energy range. Visible continuum emission, similarly aligned with the holographic kernels, reinforces the hypothesis, based on similar instances in other seismically active flares, that heating of the photosphere contributes to the observed seismic emission, possibly as a result of back-warming by the chromospheric source of the continuum emission.

The loss of HXR observations before HXR maximum encumbers our ability to conduct a realistic comparative analysis based on timing. Nevertheless, a simultaneous rise in the HXR flux with the 17 GHz and 34 GHz radio flux suggests that roughly the same particles, relativistic electrons, produce both the radio and HXR emission. The radio signature, attributed to gyro-synchrotron emission from relativistic electrons, is highly impulsive, both at the onset and the ensuing decline phases.

Gyro-synchrotron emission from flares is often characterized by an impulsive rise followed by a rapid but sometimes only partial decline in brightness temperature. Then follows a slow decline of the remaining signature over many minutes. The latter behavior is broadly attributed to electrons that are trapped in a magnetic flux tube because they were injected into the tube in a direction that lies outside of the magnetic loss cone (Kundu *et al.*, 2001). These electrons may be scattered into the loss cone by ambient thermal electrons in the flux tube and leak into the chromosphere over a duration that depends on the scattering rate, which in turn depends on the density of ambient thermal electrons in the flux tube. Whether these temporarily trapped electrons can contribute to seismic emission depends on the foregoing duration, since a significant contribution to the seismic transient is thought to depend critically on thick target heating that is relatively sudden, within about a minute or so. A rapid increase in the thermal free electron and ion density due to ablation of the upper chromosphere might facilitate the rapid injection of initially trapped relativistic electrons into the loss cone significantly increasing both the magnitude and suddenness of chromospheric and photospheric heating thought to contribute to seismic emission. Chromospheric ablation into the magnetic flux tube by relativistic

electrons initially injected into the loss cone can greatly enhance scattering by ambient electrons and ions in the magnetic flux tube, if the flux tube is filled with this material sufficiently rapidly. How rapidly this occurs must depend critically on the length of the flux tube, for example. Coronal flux tubes no more than a few Mm in length can be highly populated with dense thermal plasma within 30 seconds or so, whereas longer flux tubes would require several minutes to do so.

In the case of the flare of 14 August 2004 the decay of the 17 GHz and 34 GHz emission following the initial rise is quite rapid. This suggests that relativistic electrons are either injected predominantly into the loss cone of the magnetic flux tube at the outset or that trapped electrons not initially injected into the loss cone are scattered into it rapidly, which could enhance the seismic emission. The magnetic extrapolation of the region suggests that the field lines connecting the photospheres in the neighborhood of the seismic source to their conjugate footpoints are indeed short, only a few Mm in length. This may explain both the rapid and complete decrease in synchrotron emission following the impulsive onset and the occurrence of a relatively strong sudden white-light signature, and may help to explain a commensurate, relatively strong seismic transient emitted from a flare that otherwise is relatively weak.

References

Ambastha, A., Hagyard, M.J., and West, E.A.: 1993, *Solar Phys.* **148**, 227.

Ambastha, A., Basu, S. and Antia, H.M.: 2003, *Astrophys. J.* **218**, 151.

Ambastha, A., Basu, S., Antia, H.M., Bogart, R.S.: 2004, In: Danesy, D. (ed.), *SOHO 14 / GONG 2004 Workshop: Helio- and Asteroseismology – Towards a Golden Future, ESA SP-559*, 293.

Bastian, T.S., Benz, A.O and Gary, D.E: 1998, *Astrophys. J.* **36**, 131.

Besliu-Ionescu, D., Donea, A.-C., Cally, P. S., Lindsey, C.: 2006, In: Fletcher, K. (ed.), *SOHO-18/GONG-2006/HELAS I: Beyond the Spherical Sun, ESA SP-624* (CDROM), 67.1.

Braun, D. C.: 1995, *Astrophys. J.* **451**, 859.

Braun, D. C., Duvall, T. L. Jr. and LaBonte, B. J.: 1988, *Astrophys. J.* **335**, 1015.

Braun, D. C., and Lindsey, C., Fan, Y. and Fagan, M.: 1998, *Astrophys. J.* **502**, 968.

Braun, D. C. and Lindsey, C.: 1999a, *Astrophys. J.* **510**, 494.

Braun, D. C. and Lindsey, C.: 1999b, *Astrophys. J.* **513**, L79.

DeForest, C. E.: 2004, *Solar Phys.* **219**, 3.

Donea, A.-C., Braun, D. C. and Lindsey, C.: 1999, *Astrophys. J.* **513**, L413.

Donea, A.-C. and Lindsey, C. 2004, In Danesy, D. (ed.), *SOHO 14 / GONG 2004 Workshop: Helio- and Asteroseismology – Towards a Golden Future, ESA SP-559*, 152.

Donea, A.-C. and Lindsey, C.: 2005, *Astrophys. J.* **630**, L1168.

Donea, A.-C., Besliu D., Cally P.S., Lindsey, C.: 2005, In: Leibacher, J., Uitenbroek, H., Stein, B. (eds.), *Solar MHD: Theory and Observations - A High Spatial Resolution Perspective, Astron. Soc. Pacific Conf. Ser.* **354**, 409.

Donea, A.-C., Besliu-Ionescu, D., Cally, P. S., Lindsey, C. and Zharkova, V. V.: 2006, *Solar Phys.* **239**, 113.

Grechnev V., Kundu M., Nindos A.: 2006, *Publ. Astron. Soc. Japan* **58**, 47.

Grechnev V.: 2003, *Solar Phys.* **213**, 103.

Hudson, H. S.: 1972, *Solar Phys.* **24**, 414.

Kosovichev, A. G. and Zharkova, V. V.: 2001, *Astrophys. J.* **550**, L105.

Kosovichev, A. G. and Zharkova, V. V.: 1998, *Nature* **393**, 317.

Kundu, M.R., White, S.M., Shibasaki, k., Sakurai, T., and Grechev, V.V.: 2001, *Astrophys. J.* **547**, 1090.

Leighton, R. B., Noyes, R. W. and Simon, G. W.: 1962, *Astrophys. J.* **135**, 474.

Lindsey, C. and Braun, D. C.: 2000, *Solar Phys.* **192**, 261.

Metcalf, T. R., Alexander, D., Hudson, H. S. and Longcope, D.: 2003, *Astrophys. J.* **595**, 483.

Moradi, H. Donea, A. -C., Lindsey, C., Besliu-Ionescu, D. and Cally, P. S.: 2007, *Monthly Notices Roy. Astron. Soc.* **3**74, 1115.

Neupert, W.M.: 1968, *Astrophys. J.* **153**, L59.

Qiu, J.; Gary, D.E.: 2003, *Astrophys. J.* **599**, 615.

Sakurai T.: 1982, *Solar Phys.* **76**, 301.

Sato, J., Kosugi, T., Makishima, K.: 1999, *Publ. Astron. Soc. Japan* **5**1, 127.

Scherrer, P.H., *et al.*: 1995, *Solar Phys.* **210**, 287.

Schunker, H. J., Braun, D. C., Cally, P. S., and Lindsey, C.: 2005, *Astrophys. J.* **621**, L149.

Stein, R. F.: 1967, *Solar Phys.* **2**, 385.

Stein, R. F. and Leibacher, J. W.: 1974, *Ann. Rev. Astron. Astrophys.* **12**, 407

Sudol, J. J. and Harvey, J. W.: 2005, *Astrophys. J.* **635**, 647.

Wang, H., Liu, C., Deng, Y. and Zhang, H.: 2005, *Astrophys. J.* **627**, 1031.

Wolff, C. L.: 1972, *Astrophys. J.* **176**, 833.